


Electrocaloric Cooling Cycles in Lead Scandium Tantalate with True Regeneration via Field Variation

S. Crossley^{1,‡}, B. Nair,¹ R. W. Whatmore,² X. Moya,^{1,†} and N. D. Mathur^{1,*}

¹Materials Science, University of Cambridge, Cambridge, CB3 0FS, United Kingdom

²Department of Materials, Royal School of Mines, South Kensington Campus, Imperial College London, London SW7 2AZ, United Kingdom

 (Received 18 March 2019; revised manuscript received 30 June 2019; published 2 October 2019)

There is growing interest in heat pumps based on materials that show thermal changes when phase transitions are driven by changes of electric, magnetic, or stress field. Importantly, regeneration permits sinks and loads to be thermally separated by many times the changes of temperature that can arise in the materials themselves. However, performance and parameterization are compromised by net heat transfer between caloric working bodies and heat-transfer fluids. Here, we show that this net transfer can be avoided—resulting in true, balanced regeneration—if one varies the applied electric field while an electrocaloric (EC) working body dumps heat on traversing a passive fluid regenerator. Our EC working body is represented by bulk $\text{PbSc}_{0.5}\text{Ta}_{0.5}\text{O}_3$ near its first-order ferroelectric phase transition, where we record directly measured adiabatic temperature changes of up to 2.2 K. Indirectly measured adiabatic temperature changes of similar magnitude are identified, unlike normal, from adiabatic measurements of polarization, at nearby measurement set temperatures, without assuming a constant heat capacity. The resulting high-resolution field-temperature-entropy maps of our material, and a small clamped companion sample, are used to construct cooling cycles that assume the use of an ideal passive regenerator in order to span ≤ 20 K. These cooling cycles possess well-defined coefficients of performance that are bounded by well-defined Carnot limits, resulting in large ($>50\%$) well-defined efficiencies that are not unduly compromised by a small field hysteresis. Our approach permits the limiting performance of any caloric material in a passive regenerator to be established, optimized, and compared; provides a recipe for true regeneration in prototype cooling devices; and could be extended to balance active regeneration.

DOI: [10.1103/PhysRevX.9.041002](https://doi.org/10.1103/PhysRevX.9.041002)

Subject Areas: Condensed Matter Physics,
Materials Science

I. INTRODUCTION

Cooling technology based on vapor compression is widespread, but its reliance on environmentally harmful gases has led to growing interest in prototype heat pumps [1–17] that exploit electrocaloric (EC), magnetocaloric (MC), and mechanocaloric (mC) materials. In these materials [18,19], phase transitions—or other transitions such as those seen in relaxors [6,20,21]—are driven by changes of electric, magnetic, and stress field, respectively. By

exploiting passive [1–4,6,9,11] or active [4,7,12,13,15] regeneration, caloric materials can pump heat across temperature spans that greatly exceed the magnitude of the field-driven adiabatic temperature change ΔT in any given caloric material. In the case of passive regeneration, a nominally homogeneous caloric working body establishes a large temperature differential along a much longer column of fluid that constitutes the regenerator. In the case of active regeneration, a relatively small volume of heat-transfer fluid is used to establish a large temperature differential along both itself and a bed of caloric material(s) that constitute the regenerator. However, cooling cycles that have been hitherto proposed or realized do not display true (balanced) regeneration, because the zero-field and fixed-field temperature-dependent entropy legs are not separated by constant entropy, forcing a deleterious net transfer of heat between the caloric material and the regenerator. In the case of passive regeneration, this net-transfer problem is noted explicitly in a seminal paper [1] and elsewhere [22].

*Corresponding author.

ndm12@cam.ac.uk

†Corresponding author.

xm212@cam.ac.uk

‡Present address: Department of Applied Physics, Stanford University, Stanford, California 94305, USA.

Published by the American Physical Society under the terms of the [Creative Commons Attribution 4.0 International license](https://creativecommons.org/licenses/by/4.0/). Further distribution of this work must maintain attribution to the author(s) and the published article's title, journal citation, and DOI.

The key figure of merit for any cooling device is its coefficient of performance $\text{COP} = Q/W$, where, in each cooling cycle, net work W is done to pump heat Q from a cold load at T_c towards a hot sink at T_h . The effect of the net-transfer problem is to partially subsume regenerators into sinks or loads, with two consequences. First and foremost, it becomes impossible to realize intended cooling cycles, thus compromising device COPs. Second, the active material undergoes net heat exchange at temperatures lying away from T_c and T_h , thus compromising the calculation of the Carnot limit $T_c/(T_h-T_c)$ using measured values of T_c and T_h . Given that COPs and Carnot limits are thus compromised, it immediately follows that device efficiencies are neither optimized nor accurate (efficiency = COP/Carnot). To solve the net-transfer problem, we construct balanced cooling cycles on detailed field-temperature-entropy maps, and we accurately evaluate the resulting COPs, Carnot limits, and efficiencies. These parameters contrast with COPs for materials in isothermal cycles [23] and the related parameter of materials efficiency [24] that describes reversible caloric transitions driven isothermally in just one direction.

The net-transfer problem has been hitherto masked in EC cooling cycles, because the zero-field and fixed-field temperature-dependent entropy legs are rendered straight and parallel by assuming peak performance at all points in any given cycle [25–27]. However, even for relaxors that show large EC effects over wide ranges of temperatures [6,20,21], this assumption is reasonable only for small temperature spans T_h-T_c that would be useful only when exploiting converse EC effects for pyroelectric energy harvesting [28]. The net-transfer problem has also been masked in cooling cycles based on mC materials, either by likewise assuming peak performance [29] or by assuming isothermal conditions [23]. In the larger body of work on MC cooling, identifying zero-field and maximum-field temperature-dependent entropy legs [1,22,30–32] was not sufficient to solve the net-transfer problem, reflecting the need for field variation during regenerator transit.

Three solutions to the net-transfer problem have been hitherto proposed for MC materials, but they seem far from perfect. First, one could engineer a composite MC material that displays a large and constant isothermal entropy change over the target temperature span [33], but this solution would be laborious and require a large number of component materials to approach perfection. Second, one could exploit serendipity under very specific circumstances, as shown using entropy-temperature data that are obtained for intermediate fields using a mean-field model [34], but these circumstances are too restrictive to be of any practical value. Third, one could hold sample magnetization constant during regenerator transit [35], but this solution is experimentally unrealistic (and does not account for the small variation of sample entropy with temperature).

In this paper, we demonstrate a general solution to the net-transfer problem by constructing cooling cycles in which no net heat is exchanged between a homogeneous working body of the archetypal EC material $\text{PbSc}_{0.5}\text{Ta}_{0.5}\text{O}_3$ (PST) [2,18,36–39] and an ideal hypothetical regenerator that it traverses in order to achieve a large temperature span $T_h-T_c \gg |\Delta T|$. The underlying principle is that the two regenerator-transit legs of a given cooling cycle can be made to differ by a constant entropy if the field applied during the finite-field leg is varied according to a detailed $E(T, S')$ map of the highly reversible phase transition at finite fields above the Curie temperature $T_C \sim 295$ K, where E denotes the electric field, T denotes the temperature, and S' denotes entropy S after subtracting the zero-field entropy at our base temperature of 285 K. In contrast with the highly restrictive solutions discussed above [33–35], our strategy for true regeneration via field variation can be readily achieved by modifying standard cooling cycles. Here, we modify Brayton cycles, which are based on adiabatic EC effects, and commonly employed in prototypes.

The $E(T, S')$ maps are detailed and accurate enough to identify the field variation required for true regeneration, because they are derived by implementing the well-known [18] indirect (Maxwell) method with a range of improvements that we explain in Sec. IV. The two most notable improvements are as follows. First, our electrical polarization data are acquired at measurement set temperatures whose separation is 2 orders of magnitude less than the 10 K separation of standard practice [20,40]. Second, we evaluate the adiabatic temperature change versus the starting temperature without assuming some constant value of the specific heat capacity [18]. Our improved implementation of the indirect method results in detailed maps of $|\Delta T(S', E)|$ that we corroborate by measuring the temperature change directly with a thermocouple. Adding the starting temperature yields maps of absolute temperature $T(S', E)$, and permuting the variables yields maps of the entropy state function $S'(T, E)$. The resulting maps of $|\Delta S(T, E)|$ show a strong temperature dependence that is responsible for the regeneration imbalance in cycles with zero-field and fixed-field temperature-dependent entropy legs. The resulting maps of $E(T, S')$ permit the construction of cooling cycles with true regeneration via field variation. For all of the aforementioned color maps, we present selected cross sections in Supplemental Material [41], permitting numerical values to be read with ease.

Our cycle efficiencies are found to exceed approximately 50% even for our largest temperature span of $T_h-T_c = 20$ K and even after accounting for the small field hysteresis of the transition. Similar efficiencies are also obtained for a small volume of PST. This sample is clamped by its unelectroded surroundings and could withstand larger electric fields. Consequently, it displays a wider temperature range of operation and per unit volume of PST would be able to pump more heat from some load in each

cycle. Our PST cycle efficiencies represent accurate upper bounds on the efficiencies of EC prototypes were they to be based on our material, and the large magnitude of these efficiencies reveals that EC cooling is an intrinsically efficient process. In the future, our approach should permit an accurate comparison of caloric materials, assuming the use of ideal regenerators. Moreover, our approach should improve the parameterization and performance of regenerative cooling cycles.

II. RESULTS

PST is fabricated as described in Sec. IV. Dielectric measurements confirm the expected first-order ferroelectric phase transition at $T_C \sim 295$ K, with a small hysteresis of 2.6 K, and low dielectric loss [Fig. 1(a)]. Increasing the measurement frequency from 100 Hz to 100 kHz increases the temperature of the dielectric peak by just 1 K (Fig. S1 [41]), consistent with relaxor behavior being suppressed [37] by our high degree of B-site cation order (approximately 0.80).

The first-order phase transition is also seen in the specific heat capacity $c(T)$ measured on heating [Fig. 1(b)], from which we evaluate entropy $S'(T) = S(T) - S(285 \text{ K})$ on heating [Fig. 1(b)], as explained in Sec. IV. The entropy change for the full transition $|\Delta S_0| \sim 28.4 \text{ kJ K}^{-1} \text{ m}^{-3}$

(see Sec. IV) corresponds to the difference between $S'(T)$ above T_C and the background value with no transition [Fig. 1(b)]. As expected for a predominantly displacive phase transition in the solid state, $|\Delta S_0|$ is small with respect to the thermally induced changes of entropy away from the transition. These thermally induced changes are subtracted in cooling cycles that employ a regenerator [1], but the subtraction is precise only if one is able to achieve balanced regeneration.

We now use the indirect method to quantify changes of temperature that arise during our adiabatic (constant S') measurements of electrical polarization $P(E)$ with a field step of approximately 0.3 kV cm^{-1} and a maximum field of magnitude $E_{\text{max}} = 26 \text{ kV cm}^{-1}$. The resulting bipolar and unipolar plots are obtained at 252 measurement set temperatures $T(E = 0)$ that we identify every 0.16 K on heating slowly through the ferroelectric transition at 0.5 K min^{-1} . Four representative bipolar [Fig. 1(c)] and unipolar [Fig. 1(d)] plots form part of the full dataset that appears in Fig. S2 [41]. The four bipolar plots show that the ferroelectric loop at 280 K becomes a double loop [42] over a limited range of temperatures above T_C , evidencing the field-driven transition in PST [36]. However, we use our unipolar plots in what follows, because the field hysteresis is smaller. The temperature

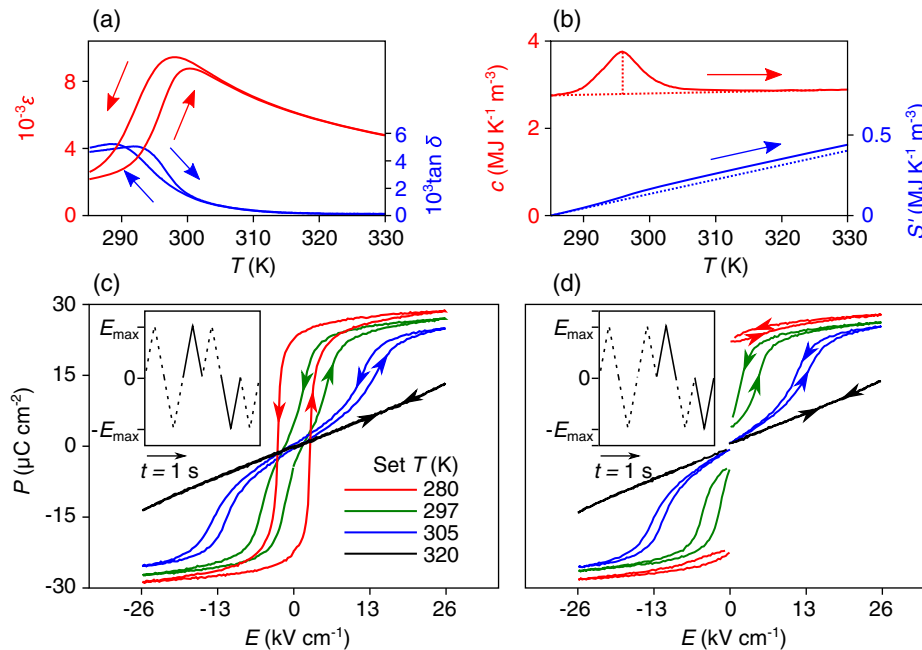


FIG. 1. The thermally and electrically driven transition in PST. (a),(b) The zero-field phase transition. (a) Relative dielectric constant ϵ and loss tangent $\tan \delta$ versus temperature T . (b) Specific heat capacity $c(T)$ (red); dotted lines denote the baseline and peak. Hence, entropy $S'(T) = S(T) - S(285 \text{ K})$ (blue); the dotted line denotes linear extrapolation from below $T_C \sim 295$ K. (c),(d) Adiabatic polarization $P(E)$ with $E_{\text{max}} = 26 \text{ kV cm}^{-1}$, for selected measurement set temperatures on heating. Data for (c) bipolar and (d) unipolar plots are acquired during the times denoted by solid lines in the insets, which show driving field E versus time t . Figure S1 [41] shows the frequency dependence of ϵ . Figure S2 [41] shows bipolar and unipolar $P(E)$ plots for all 252 measurement temperatures. Data in (a), (c),(d) are for sample A. Data in (b) are for sample E.

and entropy are interconverted at zero field from the heating branch of $S'(T)$ [Fig. 1(b)], such that an electric field modifies $S'(T)$ without entering the thermally hysteretic region.

For each sign of field, the field-application branches of our unipolar $P(E)$ plots at 252 values of S' are transposed to yield $P(S')$ plots at 100 values of E , after identifying these 100 values of E by linearly interpolating between

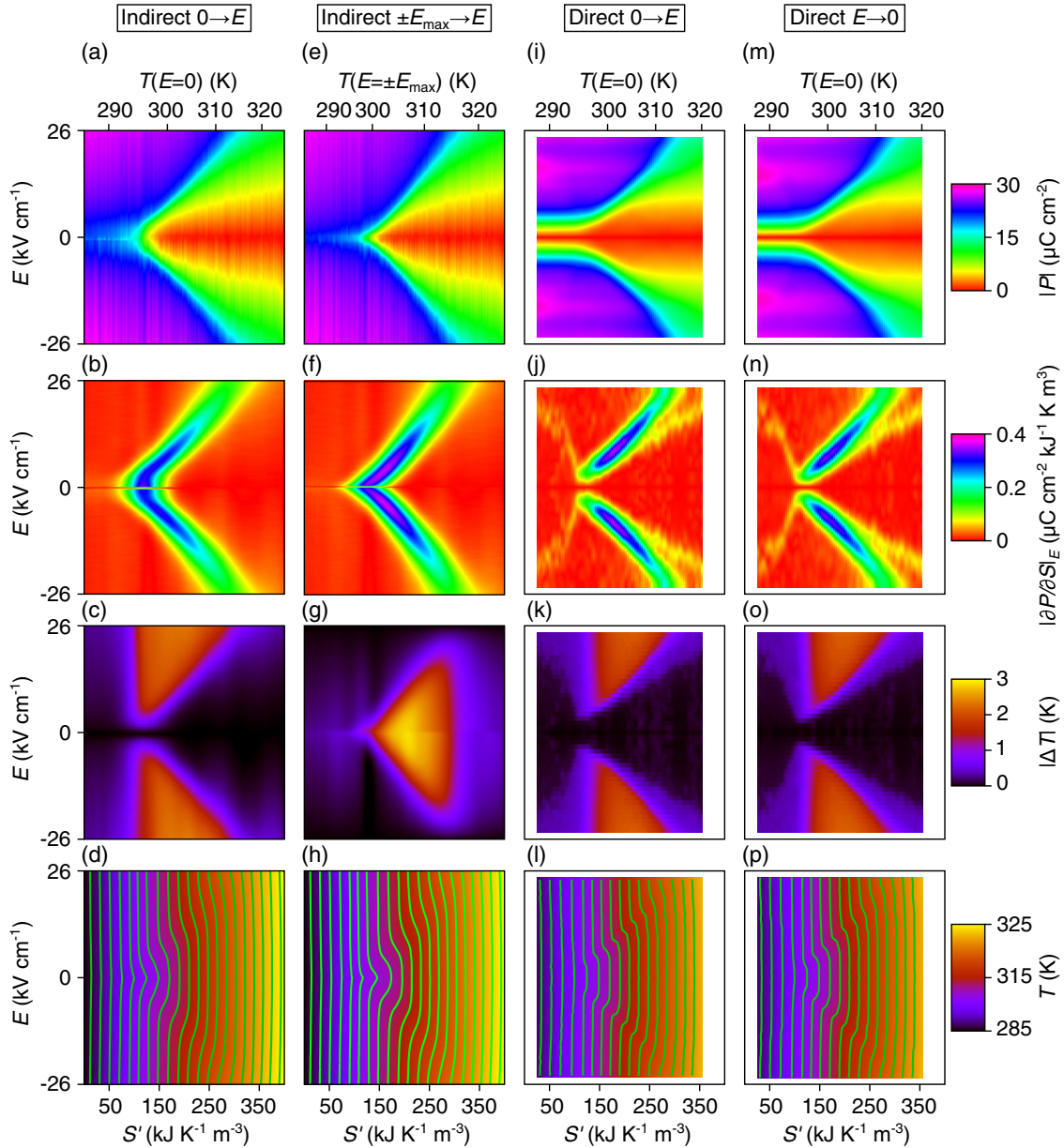


FIG. 2. PST polarization and temperature on axes of entropy and field. (a)–(h) Data based on indirect EC measurements for (a)–(d) $0 \rightarrow E$ and (e)–(h) $\pm E_{\max} \rightarrow E$. (a),(e) For each sign of field, $|P(S', E)|$ is constructed by plotting 100 isofield cubic spline fits $P(S')$ to (a) field-application branches ($0 \rightarrow E$) and (e) field-removal branches ($\pm E_{\max} \rightarrow E$) of 252 unipolar $P(E)$ plots (Fig. S2 [41]) obtained on heating at measurement set temperatures separated by 0.16 K. The resulting plots of (b),(f) $|\partial P/\partial S|_E$ imply nominally reversible adiabatic temperature changes of (c),(g) $|\Delta T(S', E)|$ starting at (c) $T(E=0)$ and (g) $T(E=\pm E_{\max})$. Hence, (d),(h) $T(S', E)$. (i)–(p) Data based on direct EC measurements for (i)–(l) field application ($0 \rightarrow E$) and (m)–(p) field removal ($E \rightarrow 0$). We identify (j),(n) $|\partial P/\partial S|_E$ and hence (i),(m) $|P(S', E)|$ from (k),(o) the directly measured temperature change $|\Delta T(S', E)|$ with respect to equilibrium temperature $T(E=0)$, which we also use to identify (l),(p) $T(S', E)$. All direct measurements of temperature change (Fig. S3 [41]) are obtained for $E > 0$, such that all data in (i)–(p) are mirrored at a negative field. (d),(h),(l),(p) Isothermal contours approximately every 1.7 K represent every third direct measurement set temperature. Data in (a)–(h) are for sample A with $E_{\max} = 26$ kV cm $^{-1}$. Data in (i)–(p) are for sample C with $E_{\max} = 24.5$ kV cm $^{-1}$. (a)–(p) Variation of starting temperature (top abscissae) with entropy S' (bottom abscissae) from $S'(T)$ [Fig. 1(b)], constant-field cross sections appear in Fig. S5 [41].

83 experimental values of E that differ slightly in each measured branch. The 100 plots of $P(S')$ are smoothed using cubic spline fits and are presented as $|P(S', E)|$ [Fig. 2(a)] with the measurement set temperature $T(E = 0)$ marked on a secondary abscissa using $S'(T)$ [Fig. 1(b)]. The plot of $|P(S', E)|$ represents a first-order phase diagram, and the resulting map of $|\partial P/\partial S|_E$ [Fig. 2(b)] highlights the phase boundary along which no critical point is reached. By exploiting the Maxwell relation $(\partial T/\partial E)_S = -(\partial P/\partial S)_E$ that is relevant for adiabatic measurements of polarization (Supplemental Note 3 [41]), this latter map permits the calculation of the nominally reversible adiabatic temperature change $\Delta T(S', E) = -\int_0^E (\partial P/\partial S)_{E'} dE' > 0$ with respect to starting temperature $T(E = 0)$ due to the application of field E [Fig. 2(c)]. The two “teeth” are seen to bite at a value of S' that corresponds to $T_C \sim 295$ K, and there is a threshold field for discernible EC effects at higher starting temperatures. The addition of $\Delta T(S', E)$ to starting temperature $T(S', 0)$ [identified from $S'(T)$ in Fig. 1(b)] results in a map of absolute temperature $T(S', E)$ [Fig. 2(d)]. While following an isothermal contour on this map, one may read the isothermal entropy change $\Delta S'(T, E)$ from the entropy abscissa. The temperature for any such contour may be read at zero field via the secondary abscissa $T(E = 0)$.

Figures 2(e)–2(h) are constructed in an analogous manner to Figs. 2(a)–2(d), using the field-removal branches of our unipolar $P(E)$ data, such that the starting temperature $T(E = \pm E_{\max})$ shown on the secondary abscissa exceeds the measurement set temperature $T(E = 0)$ due to the adiabatic EC temperature change that occurs during each field-application branch [Figs. 2(c) and 2(d)]. The nominally reversible adiabatic temperature change $\Delta T(S', E) = -\int_{\pm E_{\max}}^E (\partial P/\partial S)_{E'} dE' < 0$ is mapped for $\pm E_{\max} \rightarrow E$ [Fig. 2(g)], such that it is largest for small E and, thus, complementary with respect to the “teeth” in Fig. 2(c). One might have instead expected $\Delta T(S', E)$ to be evaluated for $E \rightarrow 0$, but, in view of the small field hysteresis, this evaluation would more properly require field-removal data for multiple values of E_{\max} at each measurement temperature. In practice, the field hysteresis is too small to significantly compromise our single-valued assumption on $P(S', E)$, such that the resulting maps of absolute temperature $T(S', E)$ are similar when derived from field-application and field-removal branches [Figs. 2(d) and 2(h)].

Direct measurements of the EC temperature change in PST are performed using a thermocouple (see Sec. IV), and the resulting figure panels [Figs. 2(i)–2(p)] are ordered for ready comparison with their indirect counterparts [Figs. 2(a)–2(h)] rather than in the order that they are obtained. At a series of measurement set temperatures $T(E = 0)$ that differ by 0.5 K, we repeat the following well-known Brayton cycle with applied fields that are increased by 1.1 kV cm^{-1} for the next cycle. An adiabatic

temperature increase $\Delta T > 0$ due to field application ($0 \rightarrow E$) is followed by a slow isofield return to the measurement set temperature $T(E = 0)$, and a subsequent adiabatic temperature decrease $\Delta T < 0$ due to field removal ($E \rightarrow 0$) is likewise followed by a slow isofield return to the same measurement set temperature. All of the resulting time-dependent data appear in Fig. S3 [41]. After converting the measurement set temperature to entropy via $S'(T)$ [Fig. 1(b)], we plot $\Delta T(S', E)$ [Figs. 2(k) and 2(o)] and $T(S', E)$ [Figs. 2(l) and 2(p)] for field application [Figs. 2(k) and 2(l)] and field removal [Figs. 2(o) and 2(p)]. Our directly measured EC effects [Figs. 2(l) and 2(p)] are similar for field application and field removal, and similar to our indirectly measured EC effects [Figs. 2(d) and 2(h)]. A more detailed comparison regarding the magnitude of these EC effects appears in Supplemental Note 7 [41].

The directly measured maps of temperature change $|\Delta T(S', E)|$ [Figs. 2(k) and 2(o)] may be used to back out $|\partial P/\partial S|_E$ [Figs. 2(j) and 2(n)] and, thus, $|P(S', E)|$ [Figs. 2(i) and 2(m)], assuming at each field an integration constant of $P \sim \epsilon_0 \epsilon E$ at $S' = 350 \text{ kJ K}^{-1} \text{ m}^{-1}$, where $\epsilon = 5730$ [Fig. 1(a)] and ϵ_0 is the permittivity of free space. Electrical data of the type used to deduce EC effects via the indirect method are, therefore, themselves deduced via directly measured EC effects, with the caveat that this method cannot identify the remanent polarization of the ferroelectric phase.

Permuting the variables in all four $T(S', E)$ maps [Figs. 2(d), 2(h), 2(l), and 2(p)] results in four entropy maps $S'(T, E)$ [Figs. 3(a), 3(e), 3(i), and 3(m)]. While following an adiabatic contour on one of these entropy maps, one may read the adiabatic temperature change $\Delta T(S', E)$ from the temperature abscissa. The entropy for any such contour may be read at zero field via the secondary abscissa $S'(E = 0)$. As expected, the ambipolar phase boundary $|dE/dT| \sim 1 \text{ kV cm}^{-1} \text{ K}^{-1}$ is correctly predicted by the Clausius-Clapeyron equation $|dE/dT| = |\Delta S_0|/|\Delta P|$, given a thermally driven entropy change of $|\Delta S_0| \sim 28.4 \text{ kJ K}^{-1} \text{ m}^{-3}$ [Fig. 1(b)] and a spontaneous polarization of $|\Delta P| \sim 26 \mu\text{C cm}^{-2}$ at 280 K [Fig. 1(d)].

The four entropy maps [Figs. 3(a), 3(e), 3(i), and 3(m)] are used to map the magnitude of the reversible entropy change $|\Delta S(E, T)|$ [Figs. 3(b), 3(f), 3(j), and 3(n)] that would arise from the isothermal application or removal of field E at temperature T . The strong temperature dependence of $|\Delta S(E, T)|$ can be eliminated by varying the field, and employing this field variation during regenerator transit at finite field yields balanced regeneration. In a small range of temperatures just above T_C , the field-driven entropy change $|\Delta S(E, T)|$ at sufficiently high fields roughly corresponds to the zero-field entropy change for the thermally driven transition ($|\Delta S_0| \sim 28.4 \text{ kJ K}^{-1} \text{ m}^{-3}$). This correspondence implies that the electrically driven transition has been driven to completion, which is rare in the EC literature, and results in a reduced isothermal

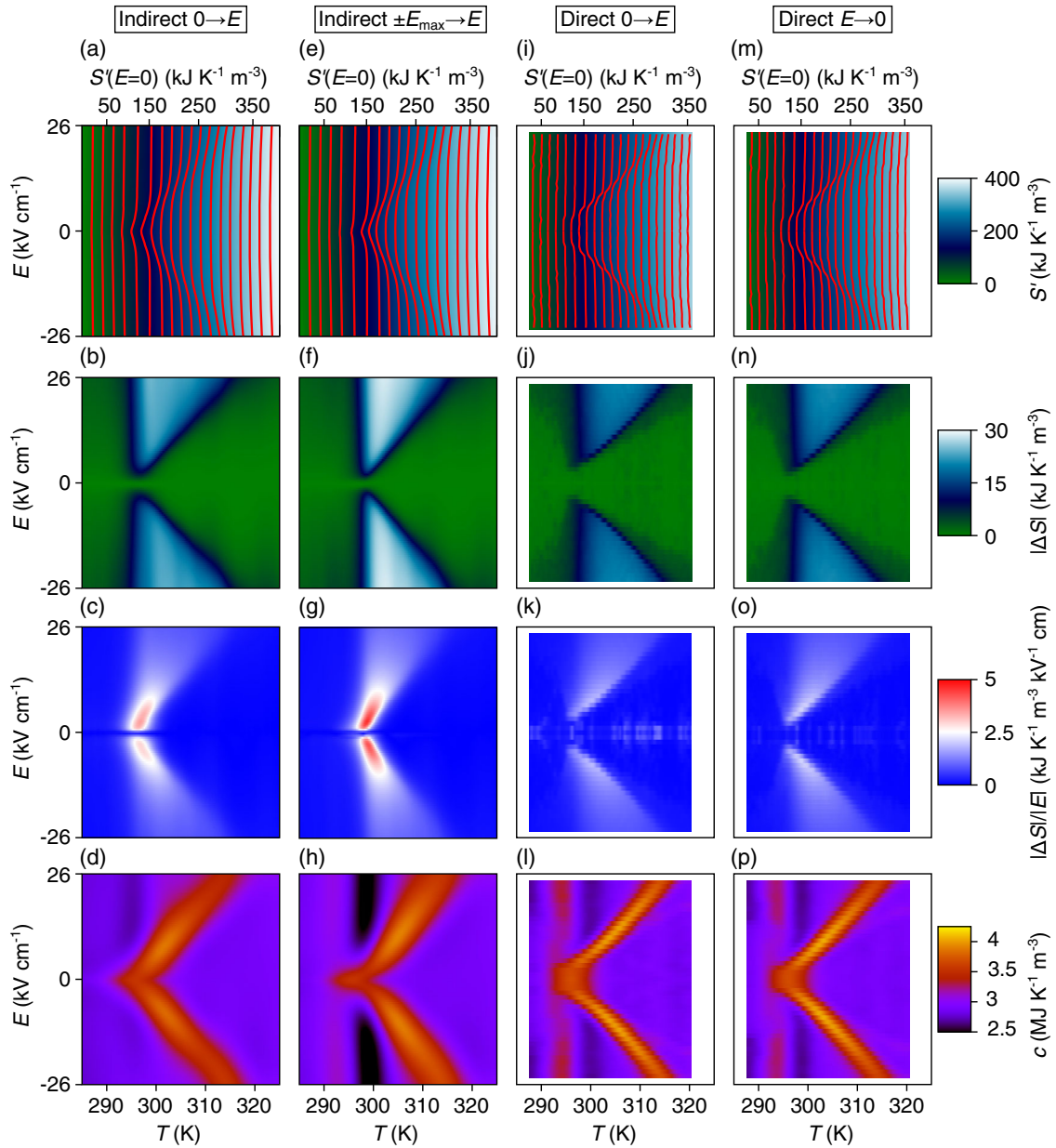


FIG. 3. PST entropy and specific heat capacity on axes of temperature and field. (a),(e),(i),(m) Entropy $S'(T, E)$ obtained by permuting the variables in $T(S', E)$ [Figs. 2(d), 2(h), 2(l), and 2(p)], with adiabatic contours approximately every $20 \text{ kJ K}^{-1} \text{ m}^{-3}$. Hence, (b),(f), (j),(n) the nominally reversible isothermal entropy change $|\Delta S(T, E)|$ for $0 \leftrightarrow E$ at temperature T . (c),(g),(k),(o) EC strength $|\Delta S(T, E)|/|E|$. (d),(h),(l),(p) Specific heat capacity $c(T, E) = T(\partial S/\partial T)_E$. (a)–(p) Constant-field cross sections appear in Fig. S6 [41].

EC strength $|\Delta S(E, T)|/|E|$ at our highest fields [Figs. 3(c), 3(g), 3(k), and 3(o)]. The persistence of a large entropy change $|\Delta S(E, T)|$ well above T_C is important, because it implies that large temperature spans $T_h - T_c$ could be achieved in regenerative devices based on PST alone. Our entropy maps permit us to identify the isofield specific heat capacity $c(E, T) = T(\partial S/\partial T)_E$ [Figs. 3(d), 3(h), 3(l), and 3(p)], which successfully captures the low-field sharpness [43] of the peak in $c(T)$, and demonstrates an equivalence between our implementation of the indirect method and the quasidirect

method [18] in which caloric effects are evaluated by measuring the field and temperature dependence of the heat capacity.

On permuting the variables in our first entropy map $S'(T, E)$ [Fig. 3(a)], which shows more conservative EC effects than its counterpart derived from field-removal data [Fig. 3(b)], we identify $E(T, S')$ [Fig. 4(a)] for positive fields above T_C in order to construct Brayton-like cooling cycles with true regeneration. For a range of load and sink temperatures (T_c and T_h), these Brayton-like cycles are parameterized while initially neglecting the small field hysteresis

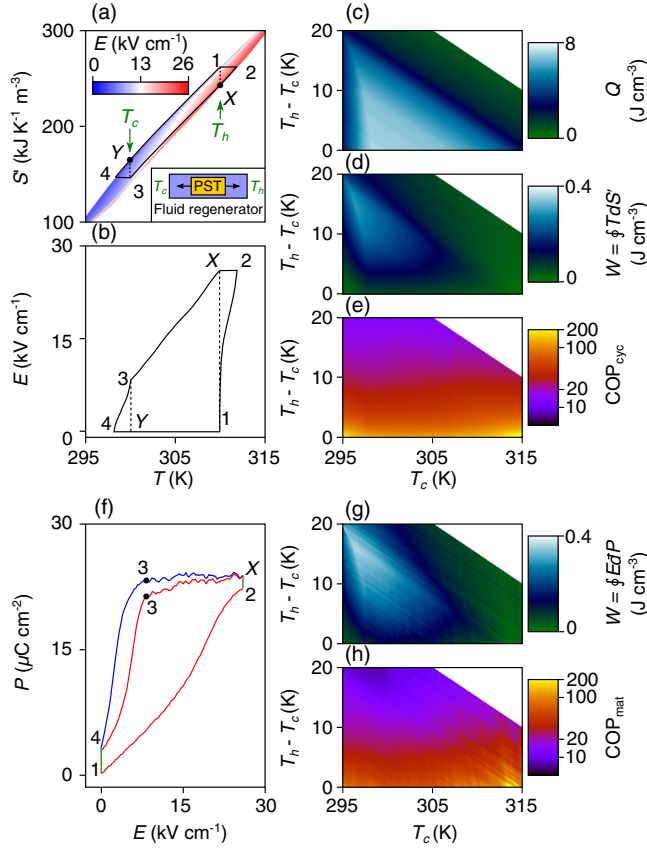


FIG. 4. Electrocaloric cooling cycles with true regeneration for PST above T_C . (a) $E(S', T)$ for $T > T_C$ and $E > 0$, obtained by permuting the variables in $S'(T, E)$ [Fig. 3(a)]. The Brayton-like balanced cooling cycle $1 \rightarrow 2 \rightarrow X \rightarrow 3 \rightarrow 4 \rightarrow Y \rightarrow 1$ with $E_{\text{max}} = 26 \text{ kV cm}^{-1}$ assumes the use of an ideal regenerator (inset). Black dotted lines show load temperature T_c and sink temperature T_h . (b) The cycle in (a) on (T, E) axes. (c)–(e) On varying T_c and $T_h - T_c$ in our cycle, we plot (c) the heat $Q = \int_4^Y T(S') dS'$ absorbed from the load at zero field, (d) cycle work $W = \oint T dS'$, and hence (e) $\text{COP}_{\text{cyc}} = Q / \oint T dS'$. (f) The cycle in (a) on (E, P) axes, with experimentally obtained data in red, isofields in green, and Y omitted for clarity. Blue data are obtained from the field-removal branches of $|P(S', E)|$ [Fig. 2(e)], resulting in an expanded cycle to account for field hysteresis. (g),(h) On varying T_c and $T_h - T_c$ for cycles thus expanded, we plot (g) work $W = \oint E dP$ and (h) $\text{COP}_{\text{mat}} = Q / \oint E dP$. Figure S7 [41] repeats (a),(b),(f) with different values of T_c and T_h . Figure S8 [41] repeats (e),(h) after dividing by the Carnot limit to obtain efficiency.

of the transition, resulting in COPs that depend purely on the choice of cycle in the accessible parameter space (these COPs are denoted COP_{cyc}). We then account for the small field hysteresis of the transition to obtain COPs that represent upper bounds for cooling devices which are based on real PST but otherwise ideal (these COPs are denoted COP_{mat}).

A Brayton-like cooling cycle ($1 \rightarrow 2 \rightarrow X \rightarrow 3 \rightarrow 4 \rightarrow Y \rightarrow 1$) with specific values of T_h and T_c is shown in Fig. 4(a). Adiabatic EC effects are driven near T_h ($1 \rightarrow 2$) and undriven near T_c ($3 \rightarrow 4$). Heat is dumped

under isofield conditions ($2 \rightarrow X$) to a sink at T_h and absorbed at zero field ($4 \rightarrow Y$) from a load at T_c . The intervening steps involve an idealized regenerator [inset, Fig. 4(a)], which heats PST from T_c to T_h during transit at zero field ($Y \rightarrow 1$) and cools PST from T_h to T_c during transit at finite field ($X \rightarrow 3$).

This finite field would assume the constant value of E_{max} if one were to follow the standard practice that results in a net transfer of heat between the EC working body and the regenerator. Here, we ensure that the regenerator and PST exchange the same heat in each half cycle by translating $Y \rightarrow 1$ down the entropy axis in order to identify $X \rightarrow 3$, such that these two legs differ by a constant entropy at all temperatures. By translating $Y \rightarrow 1$ as far down the entropy axis as possible, $X \rightarrow 3$ intersects the E_{max} isofield, thus maximizing the heat pumped from the load under the constraint of true regeneration.

The field variation required to follow $X \rightarrow 3$ [Fig. 4(a)] may be seen more clearly when the cycle is presented on (T, E) axes [Fig. 4(b)], where $1 \rightarrow 2$ and $3 \rightarrow 4$ are adiabatic contours such as those in Fig. 3(a). Presenting the cycle on (E, P) axes [red data and green isofields, Fig. 4(f)] reveals that P is fairly constant during finite-field regenerator transit $X \rightarrow 3$. Given that $P \sim 0$ during the zero-field regenerator transit $Y \rightarrow 1$, the difference of polarization between the two regenerator legs is fairly constant, as expected given that the constant entropy difference has been achieved for a range of temperatures that is too small to substantially modify phonon populations. One could therefore approximate true regeneration by maintaining constant polarization during $X \rightarrow 3$, which would, in practice, mean electrical isolation to achieve constant charge density $D \sim P$. However, it is experimentally straightforward to vary the applied field, and we seek to identify the true upper bounds on COP_{mat} , so we follow the precise recipe for true regeneration.

By varying T_h and T_c for the Brayton-like cycles $1 \rightarrow 2 \rightarrow X \rightarrow 3 \rightarrow 4 \rightarrow Y \rightarrow 1$ on our map of $E(T, S')$ [Fig. 4(a)], we plot on axes of $(T_c, T_h - T_c)$ the heat $Q = \int_4^Y T(S') dS'$ absorbed from the load [Fig. 4(c)] as calculated from the zero-field specific heat capacity data via $S'(T)$ [Fig. 1(b)]; the cycle work $W = \oint T dS'$ [Fig. 4(d)] as calculated from the area of the cycle on (T, S') axes; and thus $\text{COP}_{\text{cyc}} = Q / \oint T dS'$ [Fig. 4(e)]. Our use of reversible thermodynamics is justified, because all heat exchange with respect to the PST working body should be slow given the finite thermal time constant of the sink ($2 \rightarrow X$), the finite thermal time constant of the load ($4 \rightarrow Y$), and the need to avoid undue turbulence and friction during regenerator transit ($Y \rightarrow 1$ and $X \rightarrow 3$).

We may equally evaluate $\text{COP}_{\text{cyc}} = Q / \oint E dP$ via the cycle area on (E, P) axes [red data and green isofields, Fig. 4(f)], where electrical work $\oint E dD \sim \oint E dP$. Most of the electrical work is done ($1 \rightarrow 2$) and recovered ($3 \rightarrow 4$) when driving EC effects adiabatically, thus simplifying

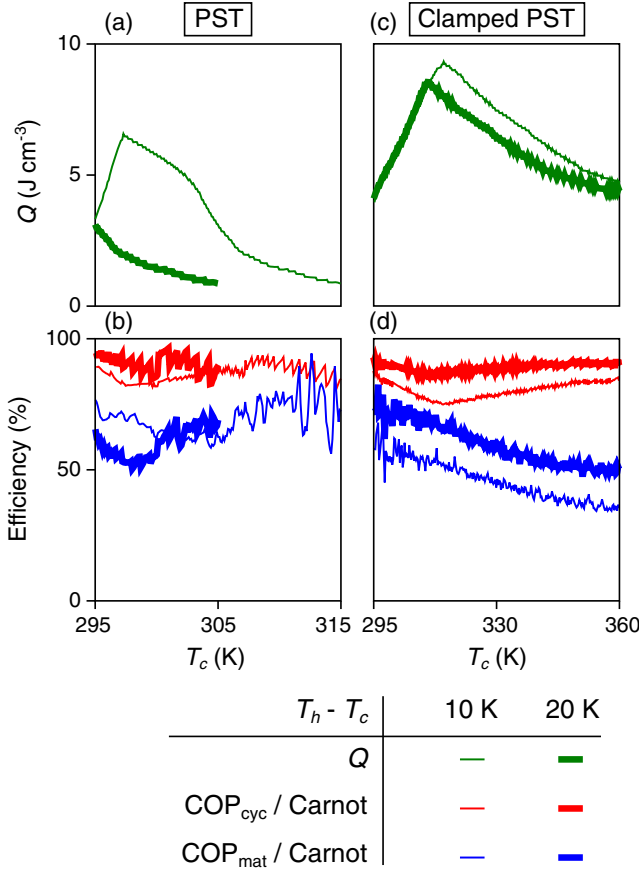


FIG. 5. Pumped heat and efficiency for PST and clamped PST. (a)–(d) For $T_h - T_c = 10$ K (thin traces) and 20 K (thick traces), we show (a) heat $Q(T_c)$ (green) and (b) cycle efficiencies $\text{COP}_{\text{cyc}}(T_c)/\text{Carnot}$ (red) and $\text{COP}_{\text{mat}}(T_c)/\text{Carnot}$ (blue), for (a),(b) PST with $E_{\text{max}} = 26$ kV cm $^{-1}$ and (c),(d) clamped PST with $E_{\text{max}} = \pm 160$ kV cm $^{-1}$. Carnot = $T_c/(T_h - T_c)$. Data for PST from Figs. 4(c), 4(e), and 4(h). Data for clamped PST from Figs. S15(c), S15(e), and S15(h) [41]. Figure S9 [41] repeats all panels with data in (b),(d) multiplied by Carnot to obtain $\text{COP}_{\text{cyc}}(T_c)$ and $\text{COP}_{\text{mat}}(T_c)$.

energy recovery [17]. We may crudely account for the small field hysteresis of the transition [Fig. 1(d)] purely by recalculating the work done to drive a given cycle whose area is increased by replacing the field-removal leg [red $X \rightarrow 4$, Fig. 4(f)] derived from the field-application branches of $|P(S', E)|$ [Fig. 2(a)] with a field-removal leg [blue $X \rightarrow 4$, Fig. 4(f)] derived from the field-removal branches of $|P(S', E)|$ [Fig. 2(e)]. The resulting values of $W = \oint E dP$ [Fig. 4(g)] slightly exceed the values of $W = \oint T dS' = \oint E dP$ [Fig. 4(d)] that are calculated without taking the field hysteresis into account (dP denotes an inexact differential). Realistic values of $\text{COP}_{\text{mat}} = Q / \oint E dP$ [Fig. 4(h)] are therefore slightly smaller than anhysteretic values of $\text{COP}_{\text{cyc}} = Q / \oint T dS'$ [Fig. 4(e)].

For useful temperature spans of $T_h - T_c = 10$ K and 20 K, cross sections through our map of Q [Fig. 4(c)] are

presented in Fig. 5(a), while the corresponding cross sections through our maps of COP_{cyc} [Fig. 4(e)] and COP_{mat} [Fig. 4(h)] are presented after dividing through by the Carnot limit to yield cycle efficiency [Fig. 5(b)]. A simple geometric construction shows that our values of $\text{COP}_{\text{cyc}}/\text{Carnot}$ fall short of the 100% that would be achieved in balanced Ericsson-like cycles $1 \rightarrow X \rightarrow 3 \rightarrow Y \rightarrow 1$ because of triangular areas $1 - 2 - X$ and $3 - 4 - Y$, which result from driving the EC effects adiabatically near T_h and T_c in our Brayton cycles. Importantly for applications, our realistic values of COP_{mat} exceed approximately 50% of the Carnot limit, suggesting that PST is a promising material for regenerative cooling devices.

To see how the embodiment of an EC material can influence COP_{mat} , we also investigate a clamped sample of PST, whose broadened phase transition is driven by order-of-magnitude larger electric fields (Supplemental Notes 11–15 [41]). Our clamped PST permits a larger volume-normalized heat Q to be achieved across a much wider temperature range [Fig. 5(c)], without significantly compromising efficiency [Fig. 5(d)]. The EC properties of PST and clamped PST are compared with other EC materials in Supplemental Note 16 [41].

COPs for a PST-based cooling device would necessarily be smaller than the values of COP_{mat} that we report here because of engineering losses such as those associated with real regenerators, those associated with the imperfect recovery [17,24] of electrical work during depolarization ($2 \rightarrow 4$), and those associated with the inactive margins of EC working bodies. However, it is encouraging to find that our values of COP_{mat} for both PST and clamped PST (12–27 for $T_h - T_c = 10$ K, 8–12 for $T_h - T_c = 20$ K) comfortably exceed the COPs for a state-of-the-art cooling device [44] based on MC gadolinium (three for $T_h - T_c = 10$ K, zero for $T_h - T_c = 20$ K). Moreover, it would be easy to vary the electric field during $X \rightarrow 3$ for true regeneration, and it would be easy to maintain a constant charge for nearly true regeneration. By contrast, it could be challenging to vary the applied magnetic field from permanent magnets for true regeneration in MC cycles, and it would presumably be even more challenging to maintain constant magnetization for nearly true regeneration [35].

III. DISCUSSION

In this paper, we obtain indirect and direct measurements of the EC effects that arise in approximately 400- μm -thick polycrystalline PST when the ferroelectric phase transition is electrically driven over a wide range of starting temperatures that lie above the Curie temperature, and we find that this range can be extended to considerably higher temperatures in a small clamped volume that could withstand larger electric fields. Our indirect and direct measurements are obtained by collecting data at nearby temperatures and fields, resulting in detailed maps that interrelate these

variables via entropy. The subsequent construction of Brayton-like cooling cycles above T_C produces three key findings. First, one may achieve true regeneration by varying the applied field when a homogeneous caloric material dumps heat on traversing an ideal fluid regenerator, such that the resulting cooling cycles are formally valid with well-defined COPs, Carnot limits, and efficiencies. Second, hysteretic losses associated with the field-driven transition are small compared with the work done to pump heat, such that our regeneratively balanced cycles are highly efficient. Third, the demonstration of large efficiencies in balanced cooling cycles demonstrates that our EC material is promising for applications.

Our work has three practical implications for the future. First, all types of caloric material should be evaluated, compared, and selected via methods of the type that we show here for PST. To recap, these methods involve collecting dense data, producing detailed maps of field on axes of entropy and temperature, choosing a range of load and sink temperatures, constructing a given type of cooling cycle with true regeneration via field variation, taking field hysteresis into account as necessary, and calculating well-defined COPs and efficiencies. Second, prototype heat pump COPs should be improved by realizing true regeneration. This improvement would involve first using detailed maps of the active caloric material in order to identify the field variation required for true regeneration with an ideal regenerator, and then refining the field variation (e.g., via machine learning) to account for engineering losses such as those we described earlier. Third, realizing true regeneration in prototype heat pumps would permit device efficiencies (COP/Carnot) to be calculated with precision. Ultimately, detailed thermodynamic maps such as those we present here could be used to identify the field variation required to balance any type of cooling cycle, including the cooling cycles used for active regeneration.

IV. METHODS

A. Sample preparation

Samples *A–E* are derived from a 0.79-mm-thick master wafer of polycrystalline $\text{PbSc}_{0.5}\text{Ta}_{0.5}\text{O}_3$ (PST), which is fabricated using the mixed-oxide method described in Ref. [45]. Specifically, Sc_2O_3 and Ta_2O_5 powders are milled together and then prereacted at 900 °C to form the wolframite phase ScTaO_4 . This phase is then reacted with PbO at 900 °C to form a single-phase perovskite powder, which is subsequently hot-pressed in Si_3N_4 tooling and an alumina grit packing medium at 40 MPa and 1200 °C for 6 h. The *B*-site cation order is inferred [46,47] to be approximately 0.80 from $|\Delta S_0| \sim 28.4 \text{ kJ K}^{-1} \text{ m}^{-3}$ [Fig. 1(b)], and we assume a density [36] of $\sim 9071 \text{ kg m}^{-3}$.

Samples *A–D* are produced by thinning, electroding, and mounting as described below, with more details in

Ref. [48], where a schematic of the entire procedure appears on page 108. Sample *E* comprises 13.249 mg of unthinned and unelectroded PST, derived from the master wafer.

Samples *A–C* are described as “PST.” Using P1200 grit polishing paper and isopropanol, these samples are fabricated by hand thinning pieces of the master wafer to a thickness of approximately 400 μm , such that sample *A* is 420 μm thick, sample *B* is 390 μm thick, and sample *C* is 450 μm thick. The concomitant reduction of applied voltage permits arcing to be avoided in our measurement probe. Sample *D* is described as “clamped PST.” It is fabricated by hand thinning a piece of the master wafer to 95 μm . P4000 paper is used to polish the side on which the bottom electrode is deposited, and P1200 and then P4000 paper are used to polish the other side.

Pt electrodes of approximate thickness 70 nm are deposited on samples *A–D* by sputtering. The bottom electrode covers the entire lower surface of each sample, while the smaller top electrode falls short of sample edges to avoid arcing. This shortfall is approximately 0.5 mm for samples *A–C* and several millimeters for sample *D*. Nominal top-electrode areas of 32 mm² (sample *A*), 39 mm² (sample *B*), and 30 mm² (sample *C*) include an approximately 6% increase for fringing fields [49]. For sample *D*, we avoid arcing by applying Apiezon “N” grease to the small top electrode, whose effective area is approximately 0.42 mm² (Supplemental Note 11 [41]).

Samples *A–D* are mounted on an electrically insulated Cu substrate using a thin layer of silver paste (samples *A–C*) or silver epoxy (sample *D*), and Kapton tape.

B. Calorimetry

Calorimetry is performed by using a TA Instruments Q2000 to heat sample *E* at 5 K min^{−1}. At temperature T , the change of entropy with respect to the absolute entropy at 285 K is evaluated via $S'(T) = S(T) - S(285 \text{ K}) = \int_{285 \text{ K}}^T c(T')/T' dT'$ [Fig. 1(b)]. The entropy change across the full transition $|\Delta S_0| = |\int_{T_1}^{T_2} c(T)/T dT| \sim 28.4 \text{ kJ K}^{-1} \text{ m}^{-3}$ is obtained after subtracting the baseline background, with T_1 set freely below the transition and T_2 set freely above the transition.

C. Electrical measurements

These are performed using a cryogenic probe that is fabricated in house [48]. Dielectric measurements are performed using an Agilent 4294A analyzer at 0.1–100 kHz while ramping the temperature at $\pm 1 \text{ K min}^{-1}$. Electrical polarization is measured on heating, using a Radiant Precision Premier II with a Trek high-voltage amplifier. Similar data are obtained on cooling [48]. All unipolar plots are positioned on the polarization axis by centering the corresponding bipolar plots.

The electrical polarization data for PST are collected under adiabatic conditions, given that the 0.25 s measurement timescale [insets in Figs. 1(c) and 1(d)] is 20 times smaller than the 5 s timescale for heat transfer that we identify from thermocouple measurements using the same cryostat (Fig. S3 [41]).

The electrical polarization data for clamped PST are also collected under adiabatic conditions, which follows because the 0.025 s measurement timescale [insets in Figs. S10(a) and S10(b)] is 10 times smaller than the 0.25 s measurement timescale for PST, while the thermal time constant is reduced by a factor of approximately 20 with respect to PST, such that the resulting measurement timescale is 10 times smaller than the resulting thermal time constant. (The thermal time constant varies quadratically with sample thickness, as the thermal resistance and thermal capacitance each vary linearly with sample thickness.)

D. Improvements to the indirect (Maxwell) method

The first of two key improvements is to acquire $P(E)$ data at nearby measurement set temperatures, thus permitting the construction of detailed $E(T, S')$ maps on which we could identify the field variation required for true regeneration. Our second key improvement is to quantify the adiabatic temperature change as a function of the starting temperature without following the standard practice [18] of assuming a constant specific heat capacity c . Instead, we generate maps of $c(T, E)$ (Fig. 3) from our $P(E)$ and $c(T)$ data.

Three other improvements to the indirect method are as follows. (i) We employ a short measurement timescale in order to obtain adiabatic rather than isothermal $P(E)$ data, thus reducing the time required for data collection. As a consequence, the adiabatic temperature change is evaluated via Maxwell relation $(\partial T/\partial E)_S = -(\partial P/\partial S)_E$ (Supplemental Note 3 [41]), using our specific heat capacity data to convert values of measurement set temperature to values of entropy. (ii) Our unipolar plots of $P(E)$ permit us to minimize field hysteresis. Moreover, unipolar cycles would likely reduce fatigue under service conditions. (iii) We obtain similar EC effects using the field-application and field-removal branches of our unipolar $P(E)$ data. This finding confirms that the single-valued assumption on $P(S', E)$ is reasonable and that the field-driven first-order phase transition is highly reversible.

E. Direct measurements of temperature change in PST

These are performed using a spot-welded K-type thermocouple, whose active junction was attached with silver paste to sample *C* at a location lying near the center of the top electrode. The two wires that represent the reference junction are each attached separately with silver paste to an insulating layer of Kapton tape, which covers the surface of the heat reservoir in the cryogenic probe

that we use for electrical measurements. Starting well above $T_C \sim 295$ K, data are obtained at measurement set temperatures approximately every 0.5 K from 320 K down to 285 K. The direction of this temperature sweep is unimportant given that the large EC effects of interest lie above T_C and are, therefore, nominally reversible [Figs. 2(k) and 2(o)].

A Keithley 2410 sourcemeter is used to apply and remove electric fields on millisecond timescales in order to drive highly adiabatic changes of temperature. However, our measured jumps in thermoelectric voltage V do not capture these temperature changes in full, for two reasons. First, the temperature of the active volume is necessarily modified by heat exchange with the thermocouple. Second, heat exchange between the active volume and the thermocouple is, in practice, accompanied by exchange heat between the active volume and the inactive material (the unaddressed PST, the sample mounting, and the very thin top electrode).

To scale our measured temperature jumps into the adiabatic limit, we establish a calibration factor of $\Delta T/\Delta V = 62.97$ K mV⁻¹ for the thermocouple by removing 15 kV cm⁻¹ from PST at ambient temperature and equating the $\Delta V = 22$ μ V recorded for sample *C* with the temperature jump of $\Delta T \sim 1.4$ K that we measure for sample *B* using scanning thermal microscopy [SThM, Fig. S4(a) [41]]. Our calibration factor exceeds the calibration factor for K-type thermocouples by a factor of 2.5 for the two reasons discussed above and is used to present all data arising from direct measurements, namely, the measured temperature changes themselves [$T(t)$, Fig. S3 [41]], the temperature jumps that we extract from these measurements [$\Delta T(S', E)$, Figs. 2(k) and 2(o)], and the resulting plots of absolute temperature [$T(S', E)$, Figs. 2(l) and 2(p)].

The aforementioned SThM measurements are performed at a tip-sample separation of 20 μ m, using an Anasys head attached to a Veeco Multimode atomic force microscope. A Keithley 3116 voltmeter was used to monitor the temperature signal at a sampling rate of kilohertz. The EC temperature change measured by SThM is assumed to be adiabatic, because the heat capacity of the sample is 7 orders of magnitude larger than the 1 nJ K⁻¹ heat capacity of the tip. The accuracy of the SThM calibration is limited by both the 0.2 K noise in the SThM data, and perhaps a small mismatch in absolute temperature with respect to the thermocouple data under calibration.

An infrared point detector (CS LT 15, Optris GmbH) is used to measure EC effects at ambient temperature as described in Ref. [48], and the results for sample *A* [Fig. S4(b)] are approximately consistent with our SThM measurements of sample *B*.

F. Cross sections through color maps

These represent a permutation of the variables for selected values of the ordinate. For example, cross sections

through a color map of $S'(T, E)$ [Fig. 3(a)] are presented as $E(T, S')$ [Fig. S6(a)] for three values of E . Repeating this procedure for all values of E yields the full map of $E(T, S')$ that we present above T_C [Fig. 4(a)].

ACKNOWLEDGMENTS

We thank P.C. Osbond for fabricating the master sample, O. Idigoras for help with sample preparation, and A.P. Carter, E. Defay, R.J. Harrison, I. Takeuchi, A. Rowe, and J. Tušek for discussions. X. M. is grateful for support from the Royal Society. B. N. is grateful for support from Gates Cambridge and the Winton Program for the Physics of Sustainability. We thank EPSRC (United Kingdom) for funding via EP/M003752/1 and the departmental Doctoral Training Account (S. C.).

-
- [1] G. V. Brown, *Magnetic Heat Pumping near Room Temperature*, *J. Appl. Phys.* **47**, 3673 (1976).
- [2] Y. V. Sinyavsky, N. D. Pashkov, Y. M. Gorovoy, G. E. Lugansky, and L. Shebanov, *The Optical Ferroelectric Ceramic as Working Body for Electrocaloric Refrigeration*, *Ferroelectrics* **90**, 213 (1989).
- [3] Yu. Sinyavsky and V. M. Brodyansky, *Experimental Testing of Electrocaloric Cooling with Transparent Ferroelectric Ceramic as Working Body*, *Ferroelectrics* **131**, 321 (1992).
- [4] B. Yu, M. Liu, P. W. Egolf, and A. Kitanovski, *A Review of Magnetic Refrigerator and Heat Pump Prototypes Built before the Year 2010*, *Int. J. Refrig.* **33**, 1029 (2010).
- [5] Y. Jia and S. J. Sungtaek, *A Solid-State Refrigerator Based on the Electrocaloric Effect*, *Appl. Phys. Lett.* **100**, 242901 (2012).
- [6] H. Gu, X. Qian, X. Li, B. Craven, W. Zhu, A. Cheng, S. C. Yao, and Q. M. Zhang, *A Chip Scale Electrocaloric Effect Based Cooling Device*, *Appl. Phys. Lett.* **102**, 122904 (2013).
- [7] U. Plaznik, A. Kitanovski, B. Rožič, B. Malič, H. Uršič, S. Drnovšek, J. Cilenšek, M. Vrabelj, A. Poredoš, and Z. Kutnjak, *Bulk Relaxor Ferroelectric Ceramics as a Working Body for an Electrocaloric Cooling Device*, *Appl. Phys. Lett.* **106**, 043903 (2015).
- [8] Y. D. Wang, S. J. Smullin, M. J. Sheridan, Q. Wang, C. Eldershaw, and D. E. Schwartz, *A Heat-Switch-Based Electrocaloric Cooler*, *Appl. Phys. Lett.* **107**, 134103 (2015).
- [9] S. Qian, A. Alabdulkarem, J. Ling, J. Muehlbauer, Y. Hwang, R. Radermacher, and I. Takeuchi, *Performance Enhancement of a Compressive Thermoelastic Cooling System Using Multi-objective Optimization and Novel Designs*, *Int. J. Refrig.* **57**, 62 (2015).
- [10] M. Schmidt, A. Schütze, and S. Seelecke, *Scientific Test Setup for Investigation of Shape Memory Alloy Based Elastocaloric Cooling Processes*, *Int. J. Refrig.* **54**, 88 (2015).
- [11] D. Sette, A. Asseman, M. Gérard, H. Strozyk, R. Faye, and E. Defay, *Electrocaloric Cooler Combining Ceramic Multilayer Capacitors and Fluid*, *APL Mater.* **4**, 091101 (2016).
- [12] P. Blumenthal, C. Molin, S. Gebhardt, and A. Raatz, *Active Electrocaloric Demonstrator for Direct Comparison of PMN-PT Bulk and Multilayer Samples*, *Ferroelectrics* **497**, 1 (2016).
- [13] J. Tušek, K. Engelbrecht, D. Eriksen, S. Dall'Olio, J. Tušek, and N. Pryds, *A Regenerative Elastocaloric Heat Pump*, *Nat. Energy* **1**, 16134 (2016).
- [14] H. Ossmer, F. Wendler, M. Gueltig, F. Lambrecht, S. Miyazaki, and M. Kohl, *Energy-Efficient Miniature-Scale Heat Pumping Based on Shape Memory Alloys*, *Smart Mater. Struct.* **25**, 085037 (2016).
- [15] T. Zhang, X.-S. Qian, H. Gu, Y. Hou, and Q. M. Zhang, *An Electrocaloric Refrigerator with Direct Solid to Solid Regeneration*, *Appl. Phys. Lett.* **110**, 243503 (2017).
- [16] R. Ma, Z. Zhang, K. Tong, D. Huber, R. Kornbluh, Y. Sungtaek Ju, and Q. Pei, *Highly Efficient Electrocaloric Cooling with Electrostatic Actuation*, *Science* **357**, 1130 (2017).
- [17] E. Defay, G. Despesse, R. Faye, H. Strozyk, D. Sette, S. Crossley, X. Moya, and N. D. Mathur, *Enhanced Electrocaloric Efficiency via Energy Recovery*, *Nat. Commun.* **9**, 1827 (2018).
- [18] X. Moya, S. Kar-Narayan, and N. D. Mathur, *Caloric Materials near Ferroic Phase Transitions*, *Nat. Mater.* **13**, 439 (2014).
- [19] S. Fähler, U. K. Röbber, O. Kastner, J. Eckert, G. Eggeler, H. Emmerich, P. Entel, S. Müller, E. Quandt, and K. Albe, *Caloric Effects in Ferroic Materials: New Concepts for Cooling*, *Adv. Eng. Mater.* **14**, 10 (2012).
- [20] B. Neese, B. Chu, S.-G. Lu, Y. Wang, E. Furman, and Q. M. Zhang, *Large Electrocaloric Effect in Ferroelectric Polymers near Room Temperature*, *Science* **321**, 821 (2008).
- [21] S. G. Lu, B. Rožič, Q. M. Zhang, Z. Kutnjak, X. Li, E. Furman, L. J. Gorny, M. Lin, B. Malič, M. Kosec, R. Blinc, and R. Pirc, *Organic and Inorganic Relaxor Ferroelectrics with Giant Electrocaloric Effect*, *Appl. Phys. Lett.* **97**, 162904 (2010).
- [22] J. He, J. Chen, J. T. Wang, and B. Hua, *Inherent Regenerative Losses of a Ferroelectric Ericsson Refrigeration Cycle*, *Int. J. Therm. Sci.* **42**, 169 (2003).
- [23] J. Cui, Y. Wu, J. Muehlbauer, Y. Hwang, R. Radermacher, S. Fackler, M. Wuttig, and I. Takeuchi, *Demonstration of High Efficiency Elastocaloric Cooling with Large ΔT Using NiTi Wires*, *Appl. Phys. Lett.* **101**, 073904 (2012).
- [24] X. Moya, E. Defay, V. Heine, and N. D. Mathur, *Too Cool to Work*, *Nat. Phys.* **11**, 202 (2015).
- [25] H. Gu, B. Craven, X. Qian, X. Li, A. Cheng, and Q. M. Zhang, *Simulation of Chip-Size Electrocaloric Refrigerator with High Cooling-Power Density*, *Appl. Phys. Lett.* **102**, 112901 (2013).
- [26] H. Gu, X.-S. Qian, H.-J. Ye, and Q. M. Zhang, *An Electrocaloric Refrigerator without External Regenerator*, *Appl. Phys. Lett.* **105**, 162905 (2014).
- [27] U. Plaznik, M. Vrabelj, Z. Kutnjak, B. Malič, A. Poredoš, and A. Kitanovski, *Electrocaloric Cooling: The Importance of Electric-Energy Recovery and Heat Regeneration*, *Europhys. Lett.* **111**, 57009 (2015).
- [28] G. Sebald, E. Lefeuvre, and D. Guyomar, *Pyroelectric Energy Conversion: Optimization Principles*, *IEEE Trans. Ultrason. Ferroelectr. Freq. Control* **55**, 538 (2008).

- [29] M. P. Annaorazova, S. A. Nikitinb, A. L. Tyurinc, S. A. Akopyanc, and R. W. Myndyevc, *Heat Pump Cycles Based on the AF–F Transition in Fe–Rh Alloys Induced by Tensile Stress*, *Int. J. Refrig.* **25**, 1034 (2002).
- [30] F. C. Chen, R. W. Murphy, V. C. Mei, and G. L. Chen, *Thermodynamic Analysis of Four Magnetic Heat-Pump Cycles*, *J. Eng. Gas Turbines Power* **114**, 715 (1992).
- [31] G. Diguët, G. Lin, and J. Chen, *Performance Characteristics of Magnetic Brayton Refrigeration Cycles Using Gd, Gd_{0.74}Tb_{0.26} and (Gd_{3.5}Tb_{1.5})Si₄ as the Working Substance*, *Int. J. Refrig.* **35**, 1035 (2012).
- [32] G. Diguët, G. Lin, and J. Chen, *Performance Characteristics of a Magnetic Ericsson Refrigeration Cycle Using Gd_xDy_{1-x} as the Working Substance*, *J. Magn. Mater.* **350**, 50 (2014).
- [33] A. Smaïli and R. Chahinea, *Composite Materials for Ericsson-like Magnetic Refrigeration Cycle*, *J. Appl. Phys.* **81**, 824 (1997).
- [34] W. Dai, *Regenerative Balance in Magnetic Ericsson Refrigeration Cycles*, *J. Appl. Phys.* **71**, 5272 (1992).
- [35] G. Lin, O. Tegus, L. Zhang, and E. Brüçk, *General Performance Characteristics of an Irreversible Ferromagnetic Stirling Refrigeration Cycle*, *Physica (Amsterdam)* **344B**, 147 (2004).
- [36] L. A. Shebanov, E. H. Birks, and K. J. Borman, *X-Ray Studies of Electrocaloric Lead-Scandium Tantalate Ordered Solid Solutions*, *Ferroelectrics* **90**, 165 (1989).
- [37] L. Shebanov and K. Borman, *On Lead-Scandium Tantalate Solid Solutions with High Electrocaloric Effect*, *Ferroelectrics* **127**, 143 (1992).
- [38] L. Shebanovs, A. Sternberg, W. N. Lawless, and K. Borman, *Isomorphous Ion Substitutions and Order-Disorder Phenomena in Highly Electrocaloric Lead-Scandium Tantalate Solid Solutions*, *Ferroelectrics* **184**, 239 (1996).
- [39] L. Shebanovs, K. Borman, W. N. Lawless, and A. Kalvane, *Electrocaloric Effect in Some Perovskite Ferroelectric Ceramics and Multilayer Capacitors*, *Ferroelectrics* **273**, 137 (2002).
- [40] A. S. Mischenko, Q. Zhang, J. F. Scott, R. W. Whatmore, and N. D. Mathur, *Giant Electrocaloric Effect in Thin-Film PbZr_{0.95}Ti_{0.05}O₃*, *Science* **311**, 1270 (2006).
- [41] See Supplemental Material at <http://link.aps.org/supplemental/10.1103/PhysRevX.9.041002> for dielectric data, raw electrical polarization data, the derivation of Maxwell relations, cross-sections through color panels, comparison of indirect and direct values of $|\Delta T|$, cooling cycles with different values of T_c and T_h , a repeat of Figs. 4 and 5 with COP and efficiency interchanged, data for clamped PST, and a comparison between PST and clamped PST.
- [42] W. J. Merz, *Double Hysteresis Loop of BaTiO₃ at the Curie Point*, *Phys. Rev.* **91**, 513 (1953).
- [43] N. Novak, Z. Kutnjak, and R. Pirc, *High-Resolution Electrocaloric and Heat Capacity Measurements in Barium Titanate*, *Europhys. Lett.* **103**, 47001 (2013).
- [44] D. Eriksen, K. Engelbrecht, C. R. H. Bahl, R. Bjørk, K. K. Nielsen, A. R. Insinga, and N. Pryds, *Design and Experimental Tests of a Rotary Active Magnetic Regenerator Prototype*, *Int. J. Refrig.* **58**, 14 (2015).
- [45] P. C. Osbond and R. W. Whatmore, *High Dielectric Constant Ceramics in the PbSc_{0.5}Ta_{0.5}O₃ – PbZrO₃ System*, *Ferroelectrics* **133**, 159 (1992).
- [46] N. Setter and L. E. Cross, *The Contribution of Structural Disorder to Diffuse Phase Transitions in Ferroelectrics*, *J. Mater. Sci.* **15**, 2478 (1980).
- [47] C. G. F. Stenger, F. L. Scholten, and A. J. Burggraaf, *Ordering and Diffuse Phase Transitions in Pb(Sc_{0.5}Ta_{0.5})O₃ Ceramics*, *Solid State Commun.* **32**, 989 (1979).
- [48] S. Crossley, *Electrocaloric Materials and Devices*, Ph.D. thesis, University of Cambridge, 2013, available at <http://www.repository.cam.ac.uk/handle/1810/245063>.
- [49] C. H. Séquin, *Fringe Field Corrections for Capacitors on Thin Dielectric Layers*, *Solid State Electron.* **14**, 417 (1971).